Full Length Article

Femtosecond laser induced damage threshold incubation and oxidation in AS$_2$S$_3$ and AS$_2$Se$_3$ thin films

Kelly T. Paula [a], Nikita S. Dutta [b], Juliana M.P. Almeida [c], L.K. Nolasco [a,d], Marcelo. B. Andrade [e], Craig B. Arnold [b], Cleber R. Mendonça [a,*]

[a] *São Carlos Institute of Physics, University of São Paulo, 13560-970 São Carlos – SP, Brazil*
[b] *Department of Mechanical and Aerospace Engineering, Princeton Institute for the Science and Technology of Materials, Princeton University, NJ 08544, USA*
[c] *Federal University of São Carlos, Department of Materials Engineering, (DEMa/UFSCar), 13565-905 São Carlos – SP, Brazil*
[d] *Department of Materials Engineering, School of Engineering of São Carlos, University of São Paulo, 13563-120 São Carlos – SP, Brazil*
[e] *Physics Department, Federal University of Ouro Preto, 35400-000 Ouro Preto – MG, Brazil*

A B S T R A C T

Laser surface structuring has emerged as a versatile technology for precise and localized material processing. When dealing with femtosecond lasers, thermal effects and collateral damage are reduced due to nonlinear light-matter interaction, improving the processing. This study explores the fabrication of microstructures using femtosecond pulses on thin films of chalcogenide glasses, which can be used for photonics applications, such as waveguides, fiber lasers, and photonic crystals. Moreover, the photoinduced changes in chalcogenide glasses have opened up new possibilities in optoelectronics, data storage, and other applications. Femtosecond laser machining of amorphous thin films of As$_2$S$_3$ and As$_2$Se$_3$ using femtosecond laser pulses is investigated through various microscopy techniques and spectroscopy tools, focusing on the impact of incubation effects and controlled photo-oxidation. This research contributes to a deeper understanding of the interaction of ultrafast pulses with chalcogenide glasses, promoting further advancements in photonics and optoelectronic applications.

1. Introduction

Laser surface structuring has been the subject of significant research and development in recent years, proving a versatile technology for spatially localized processing of materials [1–3]. Novel laser-based approaches have been studied to create functional micro- and nanostructures with high precision and reproducibility, controlling important properties suitable for applications, including photonics [4–6], electronics [7–10], chemical sensors [11–13], biodevices [14,15], microfluidics [16,17], and medical systems [18].

Femtosecond laser micromachining, in particular, is favored for its ability to process various materials, such as glasses [19–27], polymers [28–32], metals [33–35], and semiconductors [36–38], with reduced thermal effects and collateral damage that can be controlled by choosing the irradiance parameters, also allowing spatial localization of the processing due to the nonlinear light-matter interactions. Furthermore, it is an alternative to standard lithographic processes, producing complex structures in a single step, with high processing speed in ambient conditions, without the need for clean rooms and photomasks.

Femtosecond laser micromachining depends largely on the process parameters, including pulse duration, wavelength, laser fluence, and number of incident laser pulses. In particular, incubation effects that arise in multipulse and high repetition rate processing scenarios has generated great interest in the damage threshold fluence, the minimum fluence required to cause optical damage [39,40]. Thus, understanding changes in the material upon fs-laser processing is of great importance for optimizing the microfabrication process, enhancing its efficiency when ultrafast lasers and high repetition rates are used.

In the context of fabricating functional microstructures using femtosecond pulses, chalcogenide glasses are excellent candidates given their prospects for photonics applications, as they present desirable properties, such as low phonon energies, low optical losses, high linear and nonlinear refractive indexes, and a broad region of infrared transparency [41–45]. These properties, combined with their low melting temperatures, make them suitable for optics, photonics, and electronics applications [46–48]. These glasses exhibit unique characteristics stemming from their different chemical compositions. Arsenic trisulfide, known for its wider bandgap and transparency in the infrared region, contrasts with arsenic triselenide, which possesses a narrower bandgap, broader transparency extending into the visible and near-infrared regions, and generally higher refractive index. Understanding these fundamental differences is crucial for tailoring the optical and thermal

---

* Corresponding author.
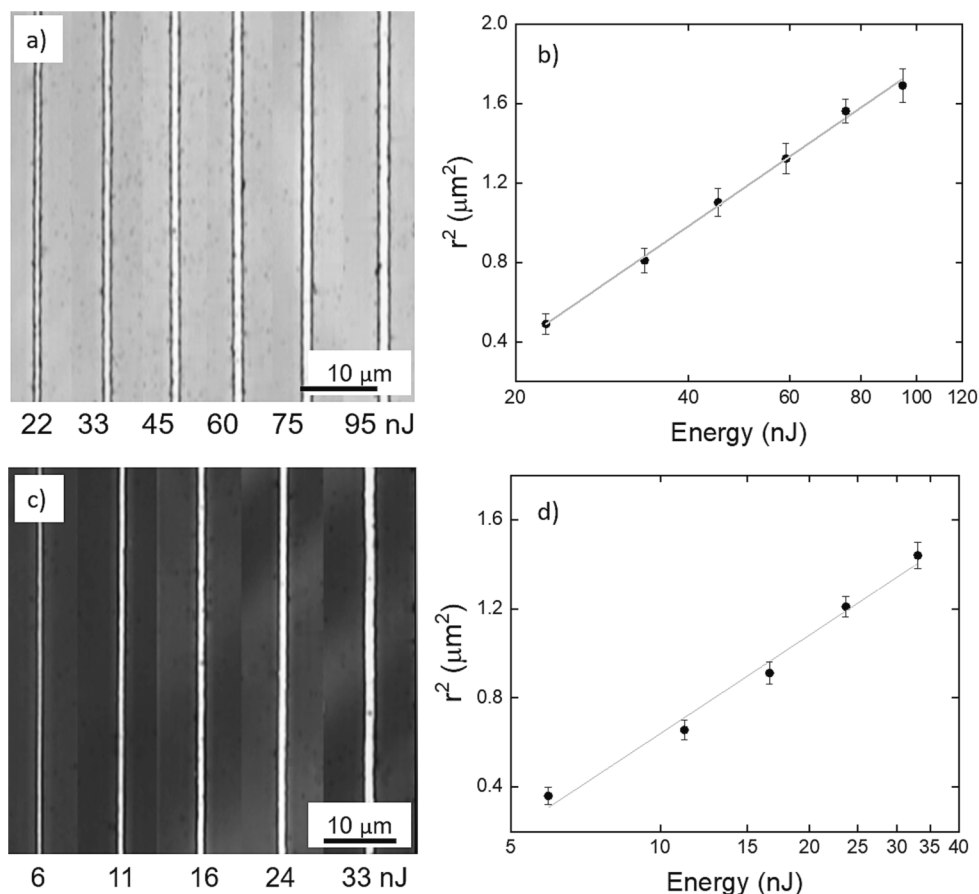*E-mail address:* crmendon@ifsc.usp.br (C.R. Mendonça).

Fig. 1. For 10 of number of pulses; a) optical images of As_2S_3 microstructures showing the evolution of the line width with the pulse energy. b) The respective line radius squares as a function of the pulse energy. c) Optical images of As_2Se_3 microstructures showing the evolution of the line width with the pulse energy. d) The respective line radius squares as a function of the pulse energy.

properties of these materials, informing their applications in areas such as infrared optics, fiber optics, and beyond. Many photonic devices based on chalcogenide glasses have been successfully fabricated by femtosecond laser micromachining, including optical waveguides [49,50], infrared fiber lasers [51], nonlinear optical switches [52], and photonic crystals [53].

Photoinduced changes in chalcogenide glasses exhibit extraordinary characteristics that have prompted further research in optoelectronics [54,55]. Recently, there has been a significant increase in exploring a wider range of applications for chalcogenide glasses, including their use in photoresists [56], optical memories[57], optoelectronic displays[58], and reconfigurable optical circuits [59]. The transition between disordered amorphous and ordered crystalline states, which can be achieved through local heating, is accompanied by electrical resistivity and optical reflectivity changes [60]. Additionally, when exposed to light, chalcogenide glasses exhibit structural and physicochemical changes, leading to photocrystallization, photopolymerization, photoexpansion, and photodissociation [61,62]. These changes can result in a distinct contrast between the two solid states, proving beneficial for data storage applications [63].

In this study, we investigated the microfabrication process of amorphous thin films of arsenic sulfide (As_2S_3) and arsenic selenide (As_2Se_3) with femtosecond laser pulses at 1030 nm, using different microscopy techniques to assess incubation effects. Moreover, controlled crystallization was achieved depending on the number of femtosecond pulses, and it was evaluated through scanning electron microscopy (SEM), energy dispersive X-ray spectroscopy (EDX), and micro-Raman spectroscopy.

2. Experimental

Chalcogenide solutions were prepared though the dissolution of arsenic trisulfide or arsenic selenide (alfa aesar 99.999 %) in propyl-amine – C_3H_9N (Sigma-Aldric > 99 %) – with a concentration of 133 g/L in a nitrogen-atmosphere glovebox. Thin films of As_2S_3 and As_2Se_3 were prepared from their respective solutions using spin-coating, typically carried out at 2000 rpm for 10——20 s onto glass coverslip as substrates. For solvent removal, the thin films were vacuum baked at 60 °C for 1 h and then at 110 °C for 7 h, resulting in films with 500 nm of thickness.

Micromachining was performed on the samples using 216-fs pulses from a diode-pumped Yb:KGW laser system, operating at a central wavelength of 1030 nm, with repetition rate in the range of 20 Hz − 200 kHz and scanning speed of 12.5 and 25 μm/s. The laser beam was focused by a 40x microscope objective (numerical aperture of 0.65) at the surface of AS_2S_3 and AS_2Se_3 films. Samples were placed in an *x-y-z* translation stage that allowed motion with constant speed in the plane perpendicular to the laser propagation. Micromachining was monitored in real-time with the aid of a CCD camera and backlight illumination, and was carried out in ambient air, under atmospheric pressure, and at room temperature.

Laser micromachining was performed using distinct pulse energies (E_o) and different numbers of pulses per spot (N), varying from 1 to ~ 20,000. N was varied by changing the laser repetition rate and scanning speed of the translational stage. For each N, groups of lines 500-μm long, separated by 10 μm, were produced to evaluate the influence of pulse energy on the line width.

The microstructures were characterized by optical microscopy using a Zeiss LSM-700 microscope, scanning electron microscopy (SEM) using
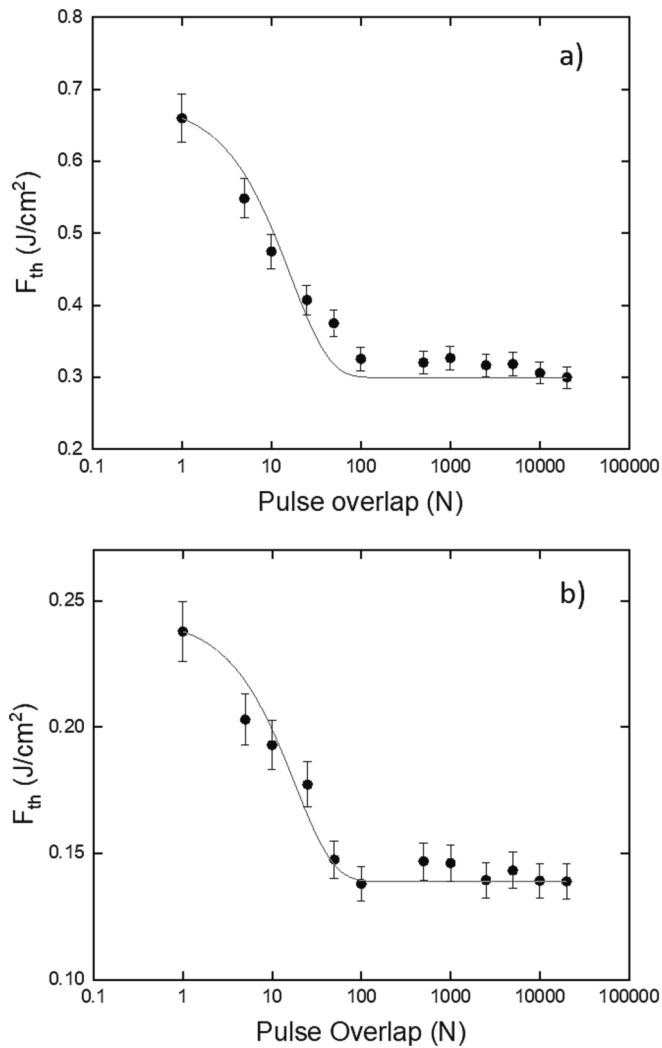
Fig. 2. Incubation curves for a) As$_2$S$_3$ and b) As$_2$Se$_3$ films. The data is fit to the exponential defect accumulation model [60] shown by the solid line.

an FEI Inspect-F50 microscope, and also by atomic force microscopy (AFM) using a Nanosurf's easyScan 2® microscope. Optical properties were analyzed by UV–Vis spectroscopy using a Shimadzu UV-1800 spectrophotometer. Raman spectra of the samples were acquired using a LabRAM HR Evolution confocal micro-Raman system with a liquid nitrogen-cooled CCD detector. Chemical analysis was conducted using Energy-dispersive X-ray spectroscopy (EDX) with a Quantax EDX-Bruker system, which was coupled to a scanning electron microscope (TM3000-Hitachi).

3. Results and discussion

Fig. 1 presents optical images of ablated lines using N = 10 and pulse energies ranging from 22 to 95 nJ (Fig. 1a) and from 6 to 33 nJ (Fig. 1c), respectively, for As$_2$S$_3$ and As$_2$Se$_3$ samples. From the optical microscopy images, it was possible to measure the half line width (r) for each group of lines, which increases with the energy. The experimental data, which presents the square of r as a function of pulse energy (E$_0$), are shown in Fig. 1b and 1d, respectively for As$_2$S$_3$ and As$_2$Se$_3$ samples. For this particular set of data (N = 10), r ranges from ~ 0.7 to 1.3 μm and from ~ 0.6 to 1.2 μm, respectively, for lines microstructured in As$_2$S$_3$ and As$_2$Se$_3$. In a larger set of experiments performed on both As$_2$S$_3$ and As$_2$Se$_3$ samples, while changing the number of pulses, the average radius varied from ~ 0.5 to 1.6 μm and from ~ 0.5 to 1.3 μm, respectively.

As the laser beam presents a Gaussian spatial distribution, it was possible to determine the threshold energy (E$_{th}$) for damage, applying the zero damage method [64] according to

$$r^2 = \frac{w_0^2}{2}\ln\left(\frac{E_0}{E_{th}}\right) \quad (1)$$

in which w_0 is the beam waist radius at the focus. By fitting the data displayed in Fig. 1b and 1d (solid lines), we have determined threshold energies of 12.8 nJ and 3.7 nJ, respectively, for As$_2$S$_3$ and As$_2$Se$_3$ ablated lines, when using N = 10. Also from the fittings, we determined the beam radius at the focus to be w$_0$ = 1.2 μm. With such values and using E$_{th}$ previously determined, we calculated the threshold laser fluence (F$_{th}$), whose values vary from 0.30 to 0.66 J/cm^2 for As$_2$S$_3$ and from 0.14 to 0.24 J/cm^2 for As$_2$Se$_3$.

We have observed a decrease in the threshold fluence with the number of pulses. This behavior is well known and commonly explained in terms of the incubation effect, being investigated in a wide range of materials, including semiconductors, metals, dielectrics, ceramics, and polymers [65–67]. Different models have been proposed to describe such an effect. Even though it is widely used for different materials, the probabilistic model of defect accumulation [39] does not provide the saturation of threshold fluence observed in Fig. 2. For this reason, the model that best describes our experimental results is the exponential defect accumulation model [68]. The model proposes that the probability of creating defects increases with the number of pulses, thus decreasing the damage threshold fluence. In this way, a constant value of the threshold fluence for a high number of pulses is established when the saturation of the defects is reached. In this model, the threshold fluence after irradiation of N pulses (F$_{th,N}$), can be related to the single pulse threshold fluence (F$_{th,1}$) and the infinite pulse threshold fluence (F$_{th,\infty}$) following the expression,

$$F_{th,N} = \left(F_{th,1} - F_{th,\infty}\right)e^{-k(N-1)} + F_{th,\infty} \quad (4)$$

where k is the incubation parameter.

The incubation curves obtained from fs-laser micromachining for As$_2$S$_3$ and As$_2$Se$_3$ are shown in Fig. 2. It Is possible to observe, for both cases, a decrease in the threshold fluence in the region from ~ 1 up to 100 pulses. This decrease in the threshold fluence ranges from 0.67 J/cm^2 to 0.32 J/cm^2 for As$_2$S$_3$, and from 0.24 J/cm^2 to 0.13 J/cm^2 for As$_2$Se$_3$, which then reaches saturation with an increasing number of pulses. By fitting the data, the incubation parameter was determined to be (0.06 ± 0.01) for As$_2$S$_3$ and (0.05 ± 0.01) for As$_2$Se$_3$, which is comparable to the values found for GaN and CVD diamond of (0.02 ± 0.01) and (0.14 ± 0.03) at 1030 nm, respectively [69]. Much like the GaN and diamond cases, the gradual change in the fluence threshold with the number of pulses suggests a low incubation parameter, indicating that a substantial quantity of pulses is necessary to induce damage to the material.

The disparity in the damage threshold fluence for the single pulse case seen in Fig. 2(a-b) for the As$_2$S$_3$ and As$_2$Se$_3$ samples can be explained by the different nonlinear ionization mechanisms present during fs-laser micromachining. Since the energy gap (E$_g$) is 2.562 eV for As$_2$S$_3$ and E$_g$ = 1.928 eV for As$_2$Se$_3$ [70,71], laser excitation at 1030 nm (1.2 eV) results in 3-photon absorption and 2-photon absorption, respectively, confirmed through the determination of the Keldysh parameter, which yielded values greater than 1.5 for both samples [72].

Nevertheless, one can extrapolate the two and three-photon cross-sections through

$$\sigma_m = \frac{2n_{cr}}{N_s\tau I_0^m}\left(\frac{hc}{\lambda}\right)^m\left(\frac{mln2}{\pi}\right)^{1/2}\exp^{-1}\left[\frac{\alpha}{4}\tau I_0\left(\frac{\pi}{ln2}\right)^{1/2}\right]$$

where the m-photon cross section is given as a function of the solid atom density (N$_s$), the Gaussian pulse peak intensity (I$_0$), the pulse duration (τ), the critical electron density (n$_{cr}$), and α, which describes the
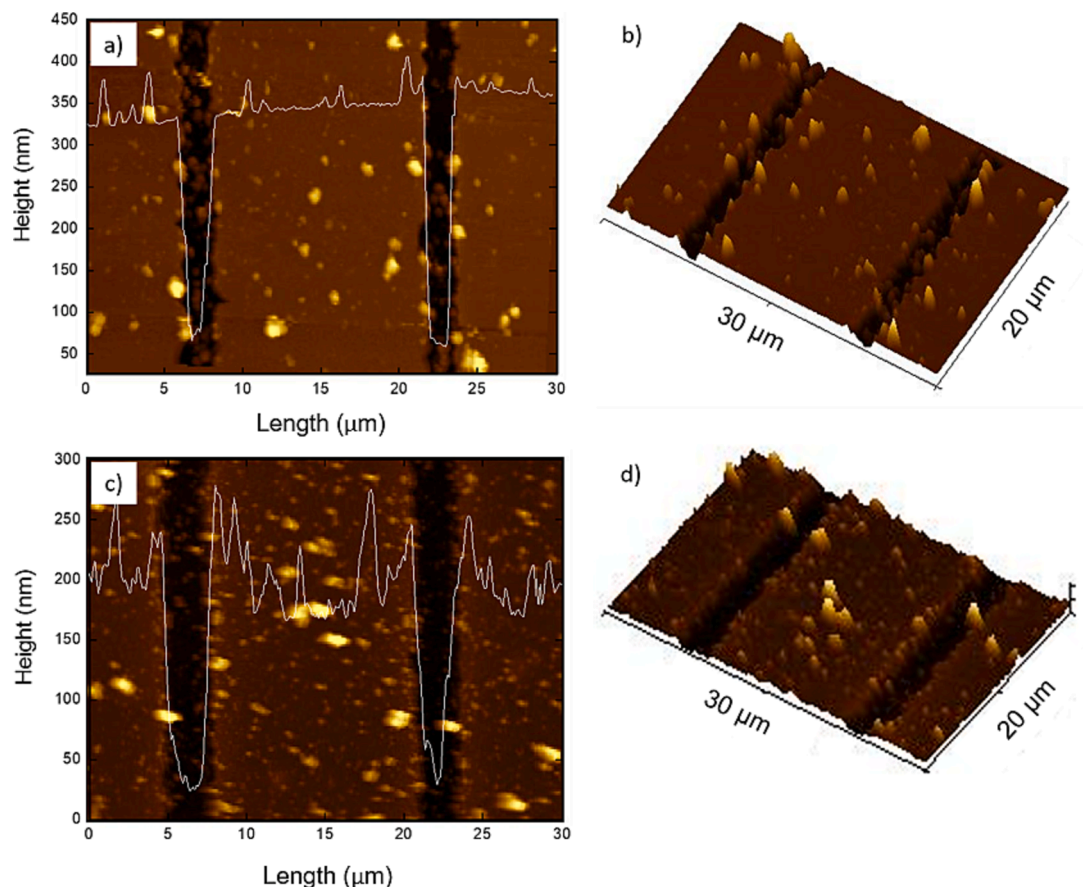
Fig. 3. A) afm image of as$_2$S$_3$ microstructure and the respective profile trace using 10 pulses, pulse energy of 60 nJ, and b) the respective AFM 3D-micrograph. c) AFM image of AS$_2$Se$_3$ microstructure and the respective profile trace using 10 pulses, pulse energy of 23 nJ, and d) the respective AFM 3D-micrograph.

avalanche ionization relevance[73]. Thus, through $F_{th,1}$ values, we determined I_0, and assuming the typical n_{cr} value of 2×10^{27} electrons/m^3 and $\alpha = 10^{-3}$ m^2/J [38,69,73,74], the cross-sections of As$_2$S$_3$ and As$_2$Se$_3$ were determined to be 2×10^{-95} m^{6}s^{2}photon^{-2} and 2×10^{-58} m^{4}s^{1}photon^{-1}, respectively.

Fig. 3a shows an AFM micrograph and trace profile of ablated lines on As$_2$S$_3$ applying 60 nJ of pulse energy and N = 10, from which we determined the depth of the lines to be approximately 300 nm. The corresponding AFM 3D-micrograph is shown in Fig. 3b. For ablated lines on As$_2$Se$_3$, applying 23 nJ of pulse energy and N = 10, we have determined a line depth of approximately 150 nm, as observed in Fig. 3c. The AFM 3D-micrograph of the ablated lines on As$_2$Se$_3$ sample is shown in Fig. 3d. From AFM results obtained for all experiments performed on As$_2$S$_3$ and As$_2$Se$_3$ samples, changing the number of pulses, the depth of the lines varied from ~ 150 to 400 nm and from ~ 100 to 200 nm, respectively, increasing with the pulse energy.

The typical Raman spectra of As$_2$S$_3$ and As$_2$Se$_3$ glasses are presented in Fig. 4a and 4b, respectively, showing the broad features characteristic of amorphous materials. The Raman spectrum of As$_2$S$_3$ exhibits a broad band at 342 cm^{-1}, which corresponds to the presence of the As-S antisymmetric stretching [75–79]. Additionally, two weak bands centered at 233 cm^{-1} and 490 cm^{-1} have been attributed to the As-As and S-S chemical bonds, respectively [80]. On the other hand, the Raman spectrum of As$_2$Se$_3$ mainly consists of a band centered at 242 cm^{-1}, which is related to the antisymmetric As-Se stretching mode [81]. There is also a weak band at 480 cm^{-1} that can be assigned to Se-Se vibrations [82].

To investigate microstructural changes between irradiated and non-irradiated regions, micro-Raman spectroscopy was employed. To complement the analyses, SEM images were also obtained for the

microfabricated structures using different energies and number of pulses. Fig. 5a presents SEM images of the As$_2$S$_3$ microstructures obtained using a pulse energy of 60 nJ for four different numbers of pulses: 20,000, 100, 5, and 1. These images cover different regions of the incubation curve. For all parameter variations, the formation of microcrystals induced by the laser pulse was observed. It is also noteworthy that by varying the pulse number, we were able to achieve control over the quantity and position of the crystals. As a result, we have achieved a controllable and uniform distribution of crystals, owing to the high resolution attained through the fs-laser micromachining process.

To confirm the presence of crystals formed by the action of femtosecond laser pulses, micro-Raman spectroscopy was performed over the range of 100 to 700 cm^{-1}. In Fig. 5b, the Raman spectrum of the microstructured line is presented for two different regions: the crystals (gray line) and the ablated area (black line). The spectrum of the ablated region, which contains the remaining material, shows the characteristic bands of As$_2$S$_3$, indicating no significant changes to the material's structure due to fs-laser pulse excitation. On the other hand, the new sharp peaks at 181, 270, 369, and 560 cm^{-1} in the gray curve confirm the crystalline nature of the structures seen in SEM images and suggest material oxidation and the crystallization of arsenic oxide [83]. The A$_{1g}$ modes may be found at 369 and 560 cm^{-1}, corresponding to an As-O-As bending vibrations [84]. Finally, there is an E$_g$ mode at 181 cm^{-1} and a T$_{2g}$ mode at 270 cm^{-1} [83].

The same behavior was observed for the microstructure of As$_2$Se$_3$. Fig. 6a shows SEM images obtained using a pulse energy of 24 nJ for four different pulse superposition numbers: 20,000, 100, 5, and 1. Similarly, for all used parameters, the formation of microcrystals induced by the laser pulse was observed. We also achieved a uniform distribution of the crystals by manipulating the laser parameters and, thus, the amount of
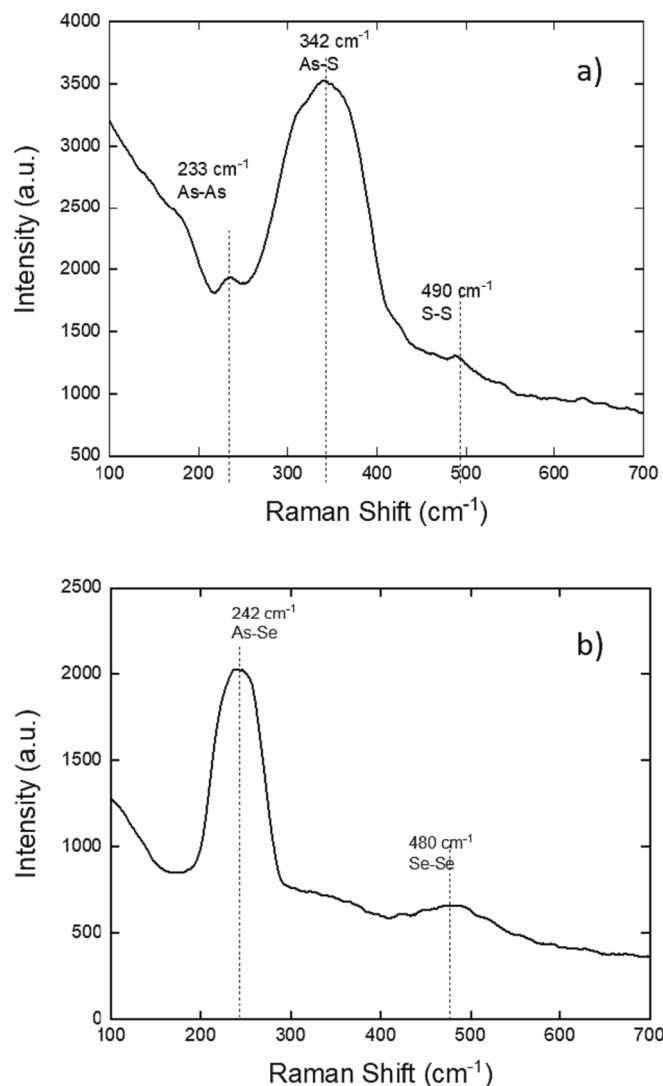
Fig. 4. Raman spectra of a) As$_2$S$_3$ film and As$_2$Se$_3$ film.

crystals. In Fig. 6b, the Raman spectrum of the microstructured line in As$_2$Se$_3$ is presented for two different regions: the crystals (gray line) and the ablated area (black line). The spectrum of the ablated region, which contains the remaining material, exhibits the characteristic bands of the As$_2$Se$_3$ film, indicating no significant changes to the material's structure due to laser excitation. The Raman spectrum of the formed crystals also exhibits alterations, with new peaks appearing at 189, 269, and 370 cm^{-1}, which are most likely related to species formed due to a photo-induced chemical reaction on the film surface [83]. These features can be attributed to the formation of arsenic oxide, as previously observed through the photo-oxidation of the material. The A$_{1g}$ mode is identified at 370 cm^{-1}, corresponding to As-O-As bending vibrations [83]. Additionally, there is an Eg mode at 189 cm^{-1} and a T$_{2g}$ mode at 269 cm^{-1} [83].

EDX analyses of the microstructures produced in As$_2$S$_3$, shown in Fig. 7, reveal that the formed microcrystals exhibit a higher concentration of oxygen and lower concentration of sulfur compared to non-irradiated regions of the film, which aligns with the Raman measurements described earlier. Berkes [85] proposed a model suggesting the occurrence of the following photochemical reaction

$$As_2S_3 \xrightarrow{h\nu} 2As + 3S. \tag{5}$$

In the presence of O$_2$ and H$_2$O, arsenic then oxidizes as follows,

$$4As + 3O_2 \xrightarrow{H2O} 2As_2O_3 \tag{6}$$

Fig. 7a displays the EDX mapping of a region within the microstructure, indicating the predominant presence of As$_2$O$_3$ crystals (Equation (6)). On the other hand, the liberated sulfur (Equation (5)) appears in smaller quantities, existing as tiny, likely crystalline, materials [85], as identified in the sulfur map shown in Fig. 7a. EDX mapping was also conducted on a single As$_2$O$_3$ crystal (Fig. 7b), revealing significant amounts of arsenic and oxygen without any sulfur. Fig. 7c presents the EDX spectrum, indicating 36 % arsenic, 54 % sulfur, and 10 % oxygen, with an experimental error of 5 %. Despite conducting measurements in various regions of Fig. 7b as indicated by 1 and 2, no other composition was observed, as it was not feasible to analyze each microcrystal individually due to their size. This suggests that the composition approximates the stoichiometric one of As$_2$S$_3$ glass, enriched in oxygen. The results presented here, caused by photo-oxidation, have been previously observed by other research groups using other types of irradiation [86–89], but without the precise control offered by femtosecond pulses.

EDX analyses of the microstructures of As$_2$Se$_3$, as shown in Fig. 8, indicate that the formed microcrystals exhibit a higher concentration of arsenic and oxygen compared to non-irradiated regions of the film, supporting the Raman measurements described earlier. Based on the proposed model, a photochemical reaction is suggested

$$As_2Se_3 \xrightarrow{h\nu} xAs + As_{2-x}Se_3 \tag{7}$$

where 0 < x < 2. In the presence of O$_2$ and H$_2$O, arsenic oxidizes in a similar manner to Equation (6).

Fig. 8a shows the EDX mapping of a region within the microstructure, indicating the presence of As$_2$O$_3$ crystals (Eq. (7)). To enhance the resolution, EDX mapping was carried out on a single As$_2$O$_3$ crystal (Fig. 8b), revealing significant amounts of arsenic and oxygen. Additionally, the presence of selenium in the crystal is evident. In contrast to As$_2$S$_3$ glass, there is a depletion of arsenic on the surface surrounding the As$_2$O$_3$ crystal, resulting in a higher selenium concentration as expected from Eq. (7), leading to the formation of Se-Se bonds around the As$_2$O$_3$ crystal [90]. Such a result is consistent with the Raman spectroscopy, which exhibits a peak at 242 cm^{-1}, attributed to different selenium atom sites [81]. Fig. 8c displays the EDX spectrum, indicating the presence of 36 % arsenic, 56 % selenium, and 8 % oxygen, with a 5 % error. Despite conducting measurements in various regions of image b in Fig. 7, as indicated by 1 and 2, no other composition was observed, as it was not feasible to analyze each microcrystal individually due to their size, indicating that the composition is approximately the stoichiometric composition of As$_2$Se$_3$ sample, enriched in oxygen, as the glass response dominates.

4. Conclusions

In this study, we demonstrate the incubation process with fs-laser pulses at 1030 nm on As$_2$S$_3$ and As$_2$Se$_3$ chalcogenide glasses. For As$_2$S$_3$, we have determined the material threshold fluence to be 0.67 J/cm^2 for a single pulse and 0.32 J/cm^2 for a large number of incident pulses on the sample. Similarly, for As$_2$Se$_3$, the material threshold fluence is 0.24 J/cm^2 for a single pulse and 0.13 J/cm^2 for a large number of pulses on the sample. Our findings reveal a small incubation factor, indicating a gradual decrease in the threshold fluence with the increasing number of pulses. In other words, a significant reduction in threshold fluence requires numerous pulses. Additionally, microscopy and spectroscopy analyses reveal the photo-oxidation of the fs-laser micromachined material with the ability to induce a localized formation of As$_2$O$_3$ crystals.
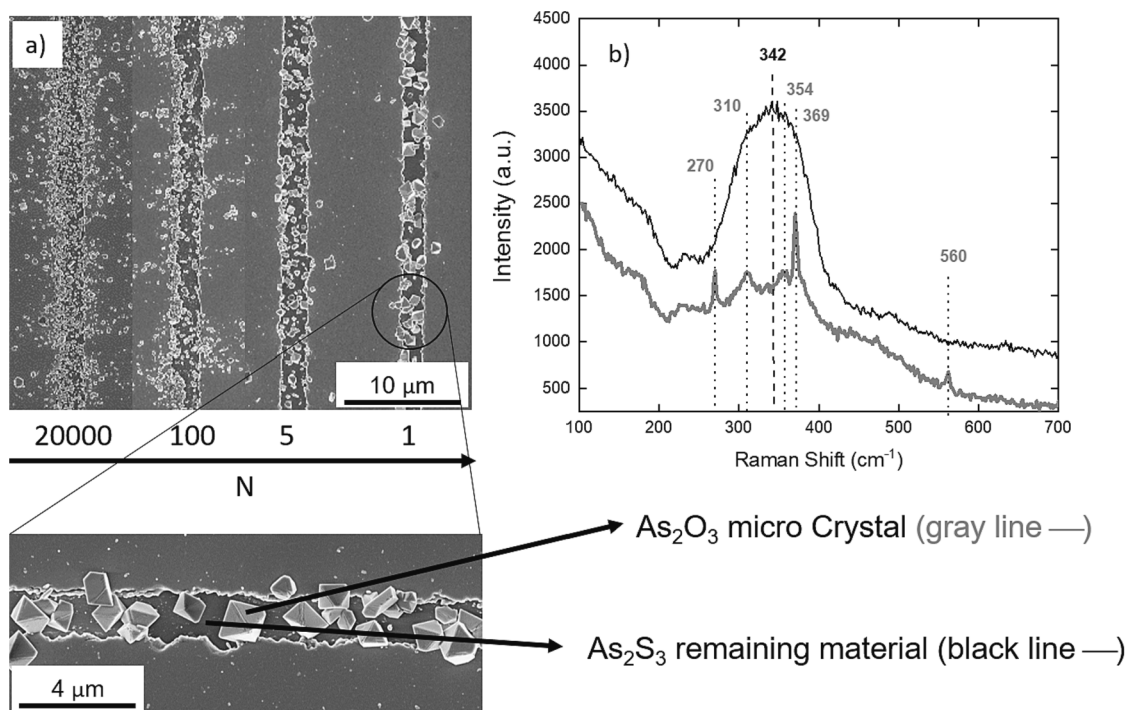
Fig. 5. A) sem images of the as$_2$S$_3$ microstructures obtained using a pulse energy of 60 nJ for four different numbers of pulses and b) Raman spectra of the microstructured line for two different regions: the crystals (gray line) and the ablated area (black line).
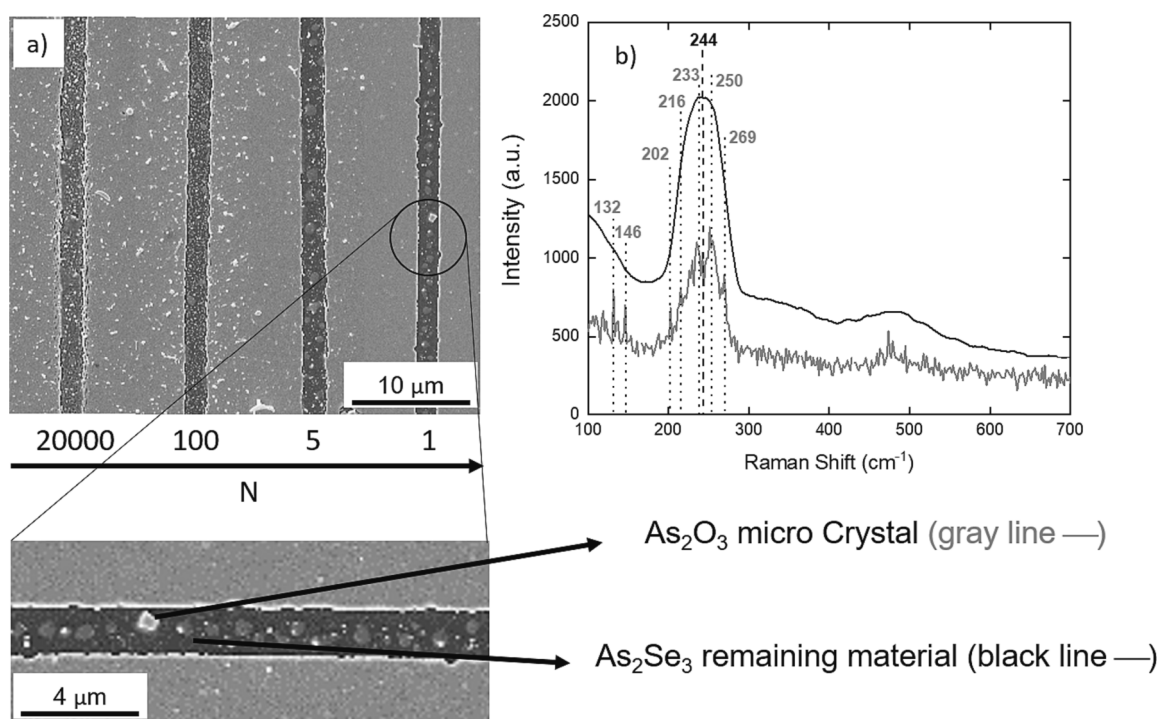

Fig. 6. A) sem images of the as$_2$Se$_3$ microstructures obtained using a pulse energy of 24 nJ for four different numbers of pulses and b) Raman spectra of the microstructured line for two different regions: the crystals (gray line) and the ablated area (black line).

CRediT authorship contribution statement

Kelly T. Paula: Writing – review & editing, Writing – original draft, Methodology, Investigation, Formal analysis, Data curation, Conceptualization. **Nikita S. Dutta:** Writing – review & editing, Resources. **Juliana M.P. Almeida:** Writing – review & editing, Resources, Methodology. **L.K. Nolasco:** Writing – original draft, Formal analysis. **Marcelo. B. Andrade:** Writing – review & editing, Data curation. **Craig B. Arnold:** Writing – review & editing, Resources, Investigation. **Cleber R. Mendonça:** Writing – review & editing, Writing – original draft, Supervision, Project administration, Methodology, Funding acquisition, Formal analysis, Conceptualization.
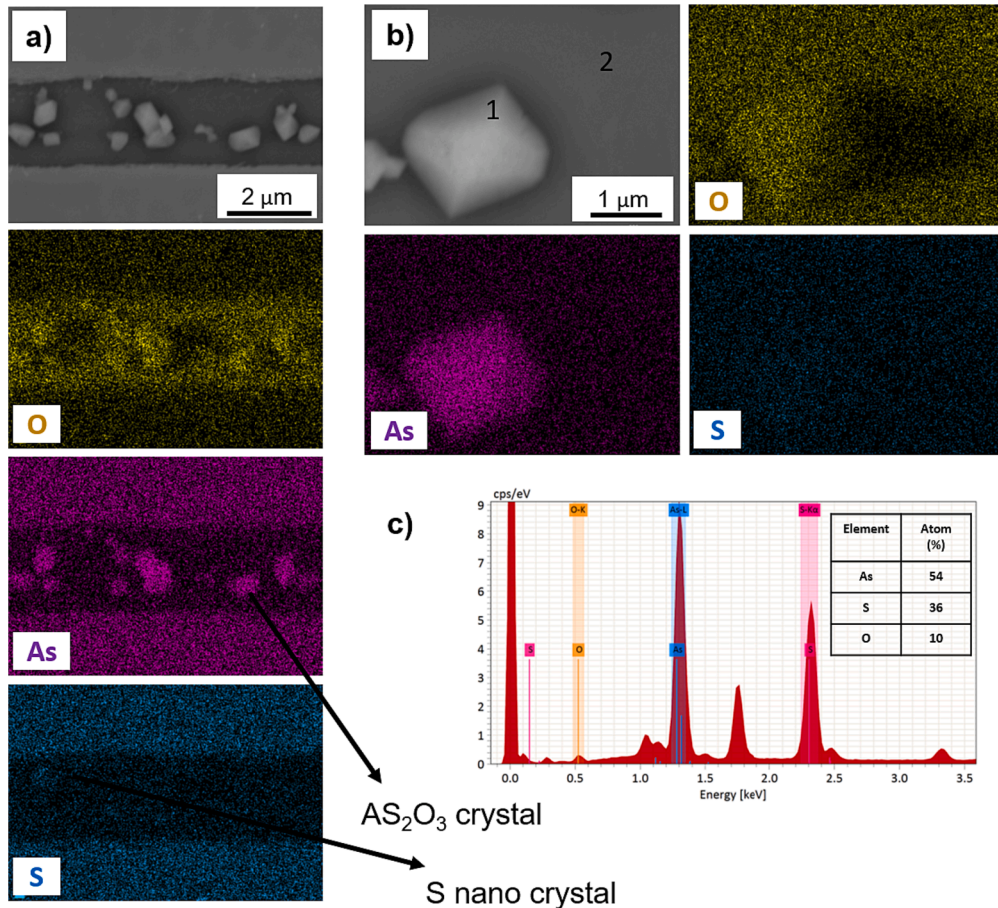
Fig. 7. a) EDX mapping of the microstructured line on As$_2$S$_3$ film. b) EDX mapping conducted on a single As$_2$O$_3$ crystal. c) EDX spectrum indicating the composition of the analyzed material.
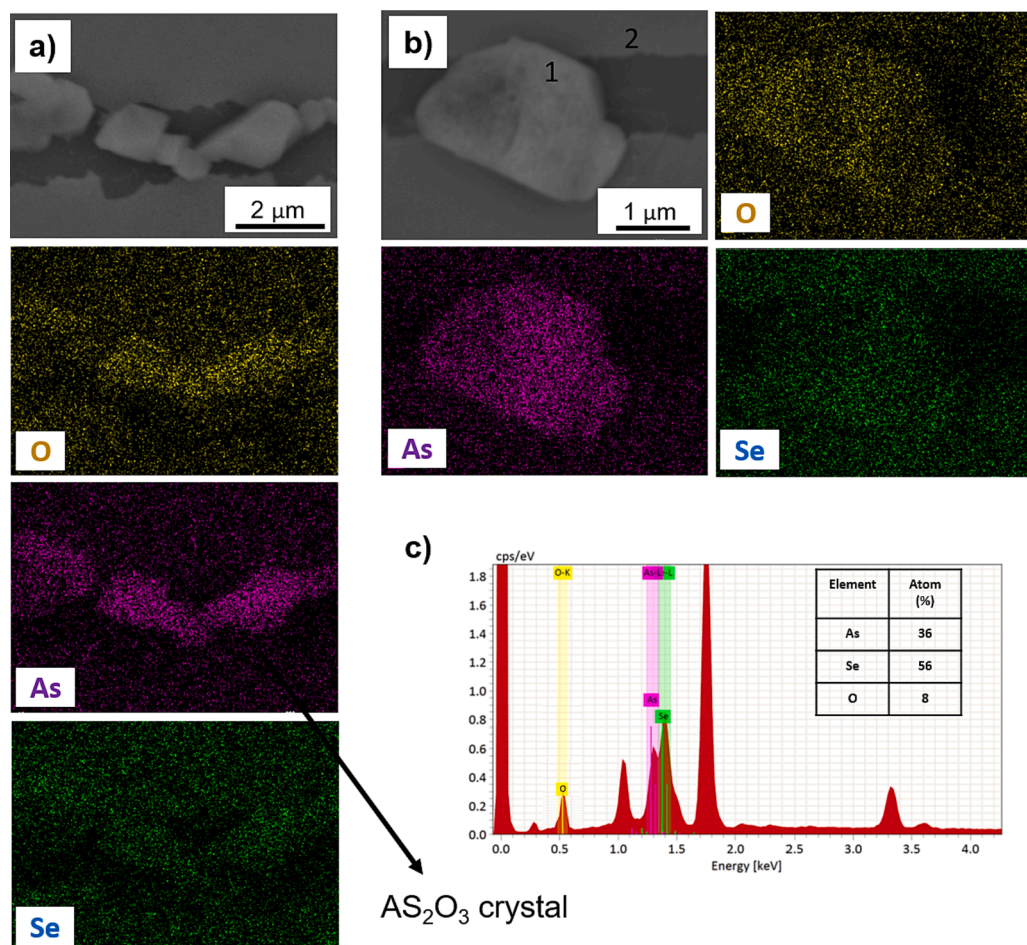
Fig. 8. a) EDX mapping of the microstructured line on As$_2$Se$_3$ film. b) EDX mapping conducted on a single As$_2$O$_3$ crystal. c) EDX spectrum indicating the composition of the analyzed material.

Declaration of competing interest

The authors declare that they have no known competing financial interests or personal relationships that could have appeared to influence the work reported in this paper.

Data availability

No data was used for the research described in the article.

References

[1] H.W. Chang, C.L. Chen, S.J. Jhu, G.W. Lin, C.W. Cheng, Y.C. Tsai, Femtosecond laser structuring in the fabrication of periodic nanostructure on titanium for enhanced photoelectrochemical dopamine sensing performance, Microchem J 187 (2023) 108423, https://doi.org/10.1016/j.microc.2023.108423.

[2] H. Wang, Q. Wang, L. Huo, J. Liu, Z. Bai, High-efficient laser-based bionic surface structuring for enhanced surface functionalization and self-cleaning effect, Surf. Interfaces 37 (2023) 102691, https://doi.org/10.1016/j.surfin.2023.102691.

[3] J.J.J. Nivas, S. He, A. Rubano, A. Vecchione, D. Paparo, L. Marrucci, et al., Direct Femtosecond Laser Surface Structuring with Optical Vortex Beams Generated by a q-plate, Sci Rep 5 (2015) 1–12, https://doi.org/10.1038/srep17929.

[4] Y.L. Sun, W.F. Dong, L.G. Niu, T. Jiang, D.X. Liu, L. Zhang, et al., Protein-based soft micro-optics fabricated by femtosecond laser direct writing, Light Sci Appl 3 (2014) 1–7, https://doi.org/10.1038/lsa.2014.10.

[5] H.B. Sun, S. Kawata, Two-photon photopolymerization and 3D lithographic microfabrication, Adv Polym Sci 170 (2004) 169–273, https://doi.org/10.1007/b94405.

[6] S.V. Makarov, V.A. Milichko, I.S. Mukhin, I.I. Shishkin, D.A. Zuev, A.M. Mozharov, et al., Controllable femtosecond laser-induced dewetting for plasmonic applications, Laser Photonics Rev 10 (2016) 91–99, https://doi.org/10.1002/lpor.201500119.

[7] E. Kymakis, K. Savva, M.M. Stylianakis, C. Fotakis, E. Stratakis, Flexible organic photovoltaic cells with in situ nonthermal photoreduction of spin-coated graphene oxide electrodes, Adv Funct Mater 23 (2013) 2742–2749, https://doi.org/10.1002/adfm.201202713.

[8] Y. Zhang, L. Guo, S. Wei, Y. He, H. Xia, Q. Chen, et al., Direct imprinting of microcircuits on graphene oxides film by femtosecond laser reduction, Nano Today 5 (2010) 15–20, https://doi.org/10.1016/j.nantod.2009.12.009.

[9] J. Zhang, K. Zhang, J. Yong, Q. Yang, Y. He, C. Zhang, et al., Femtosecond laser preparing patternable liquid-metal-repellent surface for flexible electronics, J Colloid Interface Sci 578 (2020) 146–154, https://doi.org/10.1016/j.jcis.2020.05.055.

[10] Xiaoyi Xu, Tianxin Wang, Pengcheng Chen, Chao Zhou, Jianan Ma, Dunzhao Wei, Huijun Wang, Ben Niu, Xinyuan Fang, Di Wu, Shining Zhu, Min Gu MX, YZ, Femtosecond laser writing of lithium niobate ferroelectric nanodomains, Nature 609 (2022) 496–501.

[11] Y. Zhang, X. Wang, K. Yan, H. Zhu, B.Z. Ben Wang, Laser Micro/Nano-Structuring Pushes Forward Smart Sensing: Opportunities and Challenges, Adv Funct Mater 33 (2023) 2211272.

[12] P. Sopeña, J. Arrese, S. González-Torres, J.M. Fernández-Pradas, A. Cirera, P. Serra, Low-Cost Fabrication of Printed Electronics Devices through Continuous Wave Laser-Induced Forward Transfer, ACS Appl Mater Interfaces 9 (2017) 29412–29417, https://doi.org/10.1021/acsami.7b04409.

[13] S. Papazoglou, V. Tsouti, S. Chatzandroulis, I. Zergioti, Direct laser printing of graphene oxide for resistive chemosensors, Opt Laser Technol 82 (2016) 163–169, https://doi.org/10.1016/j.optlastec.2016.03.009.

[14] C. Lai, M. Calvarese, K. Reichwald, H. Bae, M. Vafaeinezhad, T. Meyer-Zedler, et al., Design and test of a rigid endomicroscopic system for multimodal imaging and

femtosecond laser ablation, J Biomed Opt 28 (2023) 1–15, https://doi.org/10.1117/1.jbo.28.6.066004.

[15] C. Du, H. Yuan, X. Zhu, T. Zhang, Z. Liu, C. Wang, Fabrication of antibacterial Zr-BMG biomimetic surfaces by femtosecond laser, Surf. Interfaces 37 (2023) 102740, https://doi.org/10.1016/j.surfin.2023.102740.

[16] S. Sumantakul, W.E. Harley, V.T. Remcho, Laser patterned nitrocellulose-based microfluidic devices: Applications in fluid manipulation and immunoassay, Sensors Actuators B Chem 389 (2023) 133867, https://doi.org/10.1016/j.snb.2023.133867.

[17] S.S.V.T. Remcho, Selective laser ablation for in situ fabrication of enclosed channel porous-media microfluidic analytical devices, Lab Chip 23 (2023) 3194–3206.

[18] G. Buchberger, M. Muck, C. Plamadeala, J. Heitz, Laser Structuring for Biomedical Applications (2023) 1105–1165, https://doi.org/10.1007/978-3-031-14752-4_31.

[19] S.N.C. Santos, G.F.B. Almeida, J.M.P. Almeida, A.C. Hernandes, C.R. Mendonça, Waveguides fabrication by femtosecond laser in Tb3+/Yb3+ doped CaLiBO glasses, Opt Laser Technol 140 (2021) 107030, https://doi.org/10.1016/j.optlastec.2021.107030.

[20] D.M. Krol, Femtosecond laser modification of glass, J Non Cryst Solids 354 (2008) 416–424, https://doi.org/10.1016/j.jnoncrysol.2007.01.098.

[21] H. Wang, F. Zhang, K. Yin, J. Duan, Bioinspired antireflective subwavelength nanostructures induced by femtosecond laser for high transparency glass, J Non Cryst Solids 600 (2023) 122016, https://doi.org/10.1016/j.jnoncrysol.2022.122016.

[22] J.M.P. Almeida, D.S. Da Silva, L.R.P. Kassab, S.C. Zilio, C.R. Mendonça, L. De Boni, Ultrafast third-order optical nonlinearities of heavy metal oxide glasses containing gold nanoparticles, Opt Mater (amst) 36 (2014) 829–832, https://doi.org/10.1016/j.optmat.2013.12.012.

[23] D. Manzani, J.M.P. Almeida, M. Napoli, L. De Boni, M. Nalin, C.R.M. Afonso, et al., Nonlinear Optical Properties of Tungsten Lead-Pyrophosphate Glasses Containing Metallic Copper Nanoparticles, Plasmonics 8 (2013) 1667–1674, https://doi.org/10.1007/s11468-013-9585-z.

[24] J.M.P. Almeida, L. De Boni, W. Avansi, C. Ribeiro, E. Longo, A.C. Hernandes, et al., Generation of copper nanoparticles induced by fs-laser irradiation in borosilicate glass, Opt Express 20 (2012) 15106, https://doi.org/10.1364/oe.20.015106.

[25] Z. Lin, J. Xu, Y. Song, X. Li, P. Wang, W. Chu, et al., Freeform Microfluidic Networks Encapsulated in Laser-Printed 3D Macroscale Glass Objects, Adv Mater Technol 5 (2020) 1–10, https://doi.org/10.1002/admt.201900989.

[26] A. Butkutė, L. Jonušauskas, 3D Manufacturing of Glass Microstructures Using Femtosecond Laser, Micromachines (2021) 12, https://doi.org/10.3390/mi12050499.

[27] K. Sugioka, J. Xu, D. Wu, Y. Hanada, Z. Wang, Y. Cheng, et al., Femtosecond laser 3D micromachining: A powerful tool for the fabrication of microfluidic, optofluidic, and electrofluidic devices based on glass, Lab Chip 14 (2014) 3447–3458, https://doi.org/10.1039/c4lc00548a.

[28] L. Xu, W.H. Knox, Lateral gradient index microlenses written in ophthalmic hydrogel polymers by femtosecond laser micromachining, Opt Mater Express 1 (2011) 1416, https://doi.org/10.1364/ome.1.001416.

[29] M.J. Wood, M.J. Coady, F. Aristizabal, K. Nielsen, P.J. Ragogna, A.M. Kietzig, Femtosecond laser micromachining of co-polymeric urethane materials, Appl Surf Sci 483 (2019) 633–641, https://doi.org/10.1016/j.apsusc.2019.03.296.

[30] R. Ortiz, S. Moreno-Flores, I. Quintana, M.M. Vivanco, J.R. Sarasua, J.L. Toca-Herrera, Ultra-fast laser microprocessing of medical polymers for cell engineering applications, Mater Sci Eng C 37 (2014) 241–250, https://doi.org/10.1016/j.msec.2013.12.039.

[31] C.R. Mendonca, L.R. Cerami, T. Shih, R.W. Tilghman, T. Baldacchini, E. Mazur, Femtosecond laser waveguide micromachining of PMMA films with azoaromatic chromophores, Opt Express 16 (2008) 200, https://doi.org/10.1364/oe.16.000200.

[32] C.R. Mendonca, D.S. Correa, F. Marlow, T. Voss, P. Tayalia, E. Mazur et al., Three-dimensional fabrication of optically active microstructures containing an electroluminescent polymer 2009, 113309. https://doi.org/10.1063/1.3232207.

[33] X.B. Cao, L.P. Hoang, C.N.T. Kim, T.T. Vu, Laser ablation on coated metal gravures for roll-to-roll printed electronics, Opt Commun 527 (2023) 128948, https://doi.org/10.1016/j.optcom.2022.128948.

[34] K.M. Tanvir Ahmed, C. Grambow, A.M. Kietzig, Fabrication of micro/nano structures on metals by femtosecond laser micromachining, Micromachines 5 (2014) 1219–1253, https://doi.org/10.3390/mi5041219.

[35] Z. Chen, J. Yang, H. Liu, Y. Zhao, R. Pan, A short review on functionalized metallic surfaces by ultrafast laser micromachining, Int J Adv Manuf Technol 119 (2022) 6919–6948, https://doi.org/10.1007/s00170-021-08560-8.

[36] S.K. Sundaram, E. Mazur, Inducing and probing non-thermal transitions in semiconductors using femtosecond laser pulses, Nat Mater 1 (2002) 217–224, https://doi.org/10.1038/nmat767.

[37] H.J.L. Clabel, K.T. Paula, M.A. Pereira-da-Silva, J.D. Vollet-Filho, J.E. Marega, C.R. Mendonça, Fabrication of micro patterns on BaTiO3:Er3+/Yb3+ perovskite films by femtosecond laser micromachining, Appl Surf Sci 634 (2023) 157658, https://doi.org/10.1016/j.apsusc.2023.157658.

[38] L.K. Nolasco, F.A. Couto, M.B. Andrade, C.R. Mendonça, Femtosecond laser micromachining study with multiple wavelengths in CVD diamond, Diam Relat Mater 131 (2023) 109589, https://doi.org/10.1016/j.diamond.2022.109589.

[39] D. Ashkenasi, M. Lorenz, R. Stoian, A. Rosenfeld, Surface damage threshold and structuring of dielectrics using femtosecond laser pulses: the role of incubation, Appl Surf Sci 150 (1999) 101–106, https://doi.org/10.1016/S0169-4332(99)00228-7.

[40] H. Liu, W. Lin, Z. Lin, L. Ji, M. Hong, Self-Organized Periodic Microholes Array Formation on Aluminum Surface via Femtosecond Laser Ablation Induced Incubation Effect, Adv Funct Mater 29 (2019) 1903576, https://doi.org/10.1002/adfm.201903576.

[41] A. Zakery, S. Elliott, Optical properties and applications of chalcogenide glasses: a review, J Non Cryst Solids 330 (2003) 1–12, https://doi.org/10.1016/j.jnoncrysol.2003.08.064.

[42] J.H. Lee, J.H. Yi, W.H. Lee, B.J. Park, Y.G. Choi, Crystallization behavior of Ge-Sb-Se glasses in the compositional range for use as molded lenses, J Non Cryst Solids 481 (2018) 21–26, https://doi.org/10.1016/j.jnoncrysol.2017.10.017.

[43] V.S. Shiryaev, M.F. Churbanov, Recent advances in preparation of high-purity chalcogenide glasses for mid-IR photonics, J Non Cryst Solids 475 (2017) 1–9, https://doi.org/10.1016/j.jnoncrysol.2017.09.021.

[44] M. Ghayebloo, M. Rezvani, M. Tavoosi, The effect of CsI on the thermal and optical properties of IR transparent Se-S-Ge-Sb-As chalcogenide glasses, Infrared Phys Technol 108 (2020) 103352, https://doi.org/10.1016/j.infrared.2020.103352.

[45] R. Svoboda, D. Brandová, J. Málek, Thermal behavior of Ge20SeyTe80-y infrared glasses (for y up to 8 at.%), J Alloys Compd 680 (2016) 427–435, https://doi.org/10.1016/j.jallcom.2016.04.165.

[46] G.E. Snopatin, V.S. Shiryaev, V.G. Plotnichenko, E.M. Dianov, M.F. Churbanov, High-purity chalcogenide glasses for fiber optics, Inorg Mater 45 (2009) 1439–1460, https://doi.org/10.1134/S0020168509130019.

[47] A.E. Owen, J.M. Robertson, Electronic conduction and switching in chalcogenide glasses, IEEE Trans Electron Devices 20 (1973) 105–122, https://doi.org/10.1109/T-ED.1973.17617.

[48] Mehta N. Advances in Chalcogenide Glasses (ChGs): Past, Present, and Future Applications, 2023, p. 153–68. https://doi.org/10.1007/978-3-031-20266-7_5.

[49] J. Li, C. Cao, Y. Qiu, C. Kuang, X. Liu, Optical Waveguides Fabricated via Femtosecond Direct Laser Writing: Processes, Materials, and Devices, Adv Mater Technol (2023), https://doi.org/10.1002/admt.202300620.

[50] Y. Fang, C. Bao, S. Li, Z. Wang, W. Geng, Y. Wang, et al., Recent Progress of Supercontinuum Generation in Nanophotonic Waveguides, Laser Photon Rev 17 (2023), https://doi.org/10.1002/lpor.202200205.

[51] Y. Xiao, Y. He, Y. Chen, X. Xu, X. Xiao, H. Guo, Numerical modeling of multi-point side-pumped mid-infrared erbium-doped fluoride fiber lasers, Opt Express 31 (2023) 24110–24126, https://doi.org/10.1364/oe.493570.

[52] K. Yadav, R. Sangwan, M.D. Poonam, S. Sanghi, Non-linear optical properties of Sb doped InSe4 chalcogenide films for optical switching applications, J Mater Sci Mater Electron 34 (2023) 1161, https://doi.org/10.1007/s10854-023-10559-8.

[53] L. Chu Van, K. Dinh Xuan, T. Le Canh, T. Thai Doan, T. Nguyen Thi, H. Van Le, et al., Supercontinuum generation in chalcogenide photonic crystal fiber infiltrated with liquid, Opt Mater (amst) 137 (2023) 113547, https://doi.org/10.1016/j.optmat.2023.113547.

[54] K. Petkov, P.J. Ewen, Photoinduced changes in the linear and non-linear optical properties of chalcogenide glasses, J Non Cryst Solids 249 (1999) 150–159, https://doi.org/10.1016/S0022-3093(99)00330-0.

[55] A.V. Kolobov, J. Tominaga, Chalcogenide Glasses in Optical Recording: Recent Progress, J Optoelectron Adv Mater 4 (2002) 679–686.

[56] M.D. Mikhailov, A.V. Belykh, I.Y. Yusupov, Resolution ability of inorganic chalcogenide resists for hologram recording, J Opt Technol 90 (2023) 107, https://doi.org/10.1364/JOT.90.000107.

[57] A.V. Kolobov, J. Tominaga, Chalcogenide glasses as prospective materials for optical memories and optical data storage, J Mater Sci Mater Electron 14 (2003) 677–680, https://doi.org/10.1023/A:1026166701612.

[58] Z.L. Sámson, S.-C. Yen, K.F. MacDonald, K. Knight, S. Li, D.W. Hewak, et al., Chalcogenide glasses in active plasmonics, Phys Status Solidi - Rapid Res Lett 4 (2010) 274–276, https://doi.org/10.1002/pssr.201004252.

[59] S. Suresh, S. Thomas, Comprehensive review of advances in the field of chalcogenide glass microresonators, Int J Appl Glas Sci 14 (2023) 173–188, https://doi.org/10.1111/ijag.16616.

[60] P.K. Singh, D.K. Dwivedi, Chalcogenide glass: Fabrication techniques, properties and applications, Ferroelectrics 520 (2017) 256–273, https://doi.org/10.1080/00150193.2017.1412187.

[61] P. Khan, K.V. Adarsh, Light-Induced Effects in Amorphous Chalcogenide Glasses: Femtoseconds to Seconds, Physics (college Park Md) 3 (2021) 255–274, https://doi.org/10.3390/physics3020019.

[62] M.C. Rao, K. Ravindranadh, A.C. Ferdinand, M.S. Shekhawat, Physical Properties and Applications of Chalcogenide Glasses - A Brief Study, Int J Adv Pharmacy Biol Chem 2 (2013) 368–371.

[63] S. Abdollahramezani, O. Hemmatyar, H. Taghinejad, A. Krasnok, Y. Kiarashinejad, M. Zandehshahvar, et al., Tunable nanophotonics enabled by chalcogenide phase-change materials, Nanophotonics 9 (2020) 1189–1241, https://doi.org/10.1515/nanoph-2020-0039.

[64] J.M. Liu, Simple technique for measurements of pulsed Gaussian-beam spot sizes, Opt Lett 7 (1982) 196, https://doi.org/10.1364/ol.7.000196.

[65] L.D. Merkle, N. Koumvakalis, M. Bass, Laser-induced bulk damage in SiO2 at 1.064, 0.532, and 0.355 μm, J Appl Phys 55 (1984) 772–775, https://doi.org/10.1063/1.333136.

[66] R.N. Oosterbeek, C. Corazza, S. Ashforth, M.C. Simpson, Effects of dopant type and concentration on the femtosecond laser ablation threshold and incubation behaviour of silicon, Appl Phys A 122 (2016) 449, https://doi.org/10.1007/s00339-016-9969-y.

[67] F. Di Niso, C. Gaudiuso, T. Sibillano, F.P. Mezzapesa, A. Ancona, P.M. Lugarà, Influence of the repetition rate and pulse duration on the incubation effect in multiple-shots ultrafast laser ablation of steel, Phys Procedia 41 (2013) 698–707, https://doi.org/10.1016/j.phpro.2013.03.136.

[68] Z. Sun, M. Lenzner, W. Rudolph, Generic incubation law for laser damage and ablation thresholds, J Appl Phys 117 (2015), https://doi.org/10.1063/1.4913282.

[69] L.K. Nolasco, G.F.B. Almeida, T. Voss, C.R. Mendonça, Femtosecond laser micromachining of GaN using different wavelengths from near-infrared to ultraviolet, J Alloys Compd 877 (2021) 160259, https://doi.org/10.1016/j.jallcom.2021.160259.

[70] A. Patel, D. Singh, Y. Sonvane, P.B. Thakor, R. Ahuja, Bulk and monolayer As2S3 as promising thermoelectric material with high conversion performance, Comput Mater Sci 183 (2020) 109913, https://doi.org/10.1016/j.commatsci.2020.109913.

[71] A. Aparimita, C. Sripan, R. Ganesan, R. Naik, Photo- and thermally induced property change in Ag diffusion into Ag/As2Se3 thin films, Appl Phys A 124 (2018) 267, https://doi.org/10.1007/s00339-018-1692-4.

[72] C.B. Schaffer, A. Brodeur, E. Mazur, Laser-induced breakdown and damage in bulk transparent materials induced by tightly focused femtosecond laser pulses, Meas Sci Technol 12 (2001) 1784–1794, https://doi.org/10.1088/0957-0233/12/11/305.

[73] B.C. Stuart, M.D. Feit, S. Herman, A.M. Rubenchik, B.W. Shore, M.D. Perry, Nanosecond-to-femtosecond laser-induced breakdown in dielectrics, Phys Rev B 53 (1996) 1749–1761, https://doi.org/10.1103/PhysRevB.53.1749.

[74] L.K. Nolasco, F.P. Almeida, G.F.B. Almeida, J.M.P. Almeida, V.R. Mastelaro, K.T. Paula, et al., Femtosecond-laser processing incubation in Diamond-like carbon, Opt Mater (amst) 126 (2022) 112203, https://doi.org/10.1016/j.optmat.2022.112203.

[75] D.Y. Seung, A. Levasseur, M. Couzi, Preparation, infrared and Raman characterisation and electrical properties of Li2S–B2S3–As2S3 based glasses, Phys. Chem. Glas. 39 (1998) 295-300(6).

[76] M.C.R. Shastry, M. Couzi, A. Levasseur, M. Ménétrier, Raman spectroscopic studies of As 2 S 3 and Li 2 S-As 2 S 3 glasses, Philos Mag B 68 (1993) 551–560, https://doi.org/10.1080/13642819308217934.

[77] P. Kutálek, P. Knotek, A. Šandová, T. Vaculovič, E. Černošková, L. Tichý, Ablation of binary As2S3, As2Se3, GeS2, GeSe2 and GeSe3 bulk glasses and thin films with a deep ultraviolet nanosecond laser, Appl Surf Sci 554 (2021) 149582, https://doi.org/10.1016/j.apsusc.2021.149582.

[78] P. Knotek, P. Kutálek, E. Černošková, M. Vlček, L. Tichý, The density, nanohardness and some optical properties of As–S and As–Se chalcogenide bulk glasses and thin films, RSC Adv 10 (2020) 42744–42753, https://doi.org/10.1039/D0RA08939G.

[79] H.S. Min, Characterization Techniques for Metal Chalcogenide Thin Films: Review. Curr. Adv. Chem. Biochem. Vol. 1, Book Publisher International (a part of

SCIENCEDOMAIN International); 2021, p. 106–25. https://doi.org/10.9734/bpi/cacb/v1/7235D.

[80] M. Frumar, A.P. Firth, A.E. Owen, Optically induced crystal-to-amorphous-state transition in As2S3, J Non Cryst Solids 192–193 (1995) 447–450, https://doi.org/10.1016/0022-3093(95)00426-2.

[81] A. Ben Salem, R. Cherif, M. Zghal, Raman response of a highly nonlinear As 2Se 3-based chalcogenide photonic crystal fiber, Prog Electromagn Res Symp (2011) 1256–1260.

[82] E. Finkman, A.P. DeFonzo, J. Tauc, Raman Studies of the Crystallization of As2Se3. Proc. Twelfth Int, Conf. Phys. Semicond., Wiesbaden: Vieweg+teubner Verlag (1974) 1022–1026, https://doi.org/10.1007/978-3-322-94774-1_176.

[83] P.A. Guńka, M. Dranka, J. Piechota, G.Z. Zukowska, A. Zalewska, J. Zachara, As 2O 3 polymorphs: Theoretical insight into their stability and ammonia templated claudetite II crystallization, Cryst Growth Des 12 (2012) 5663–5670, https://doi.org/10.1021/cg3011579.

[84] I. Bohdanov, S. Kovachov, Y. Suchikova, A. Moskina, T. Tsebriienko, A.I. Popov, Synthesis of Diamond-Like Arsenolite Crystallites on Surface of Gallium Arsenide, 2022 IEEE 12th Int. Conf. Nanomater. Appl. Prop., IEEE, 2022, p. 01–5. https://doi.org/10.1109/NAP55339.2022.9934708.

[85] J.S. Berkes, S.W. Ing, W.J. Hillegas, Photodecomposition of amorphous As2Se3 and As 2S3, J Appl Phys 42 (1971) 4908–4916, https://doi.org/10.1063/1.1659873.

[86] K. Ogusu, T. Hagihara, Y. Hosokawa, M. Minakata, Dependence of photo-oxidation on Ag(Cu)-content in Ag(Cu)-As2Se3 films, J Non Cryst Solids 353 (2007) 1216–1220, https://doi.org/10.1016/j.jnoncrysol.2007.01.010.

[87] P. Knotek, M. Vlcek, M. Kincl, L. Tichy, On the ultraviolet light induced oxidation of amorphous As 2S 3 film, Thin Solid Films 520 (2012) 5472–5478, https://doi.org/10.1016/j.tsf.2012.03.116.

[88] E. Márquez, J.M. González-Leal, R. Prieto-Alcón, R. Jiménez-Garay, M. Vlcek, On the photo- and thermally-induced darkening phenomena in As40S40Se20 amorphous chalcogenide thin films, J Phys D Appl Phys 32 (1999) 3128–3134, https://doi.org/10.1088/0022-3727/32/24/306.

[89] T.S. Kavetskyy, Radiation-induced optical darkening and oxidation effects in As2S3 glass, Semicond Phys Quantum Electron Optoelectron 17 (2014) 308–312. https://doi.org/10.15407/spqeo17.03.308.

[90] K. Ogusu, Y. Hosokawa, S. Maeda, M. Minakata, H. Li, Photo-oxidation of As2Se3, Ag-As2Se 3, and Cu-As2Se3 chalcogenide films, J Non Cryst Solids 351 (2005) 3132–3138, https://doi.org/10.1016/j.jnoncrysol.2005.07.034.